Journal of
Materials Chemistry A

Materials for energy and sustainability

Accepted Manuscript

This article can be cited before page numbers have been issued, to do this please use: L. G. Graversen, N. Schlegel, F. B. Holde, A. Sanz Arjona, S. Punke, T. M. Nielsen, A. S. Anker, J. Forner, G. K. H. Wiberg, M. Arenz, R. K. Pittkowski and K. M. Ø. Jensen, *J. Mater. Chem. A*, 2026, DOI: 10.1039/D6TA02189A.

ROYAL SOCIETY OF CHEMISTRY

rsc.li/materials-a

View Article Online
DOI: 10.1039/D6TA02189A

Ultra-small iridium oxide nanoparticles: from one-pot hydrothermal synthesis to oxygen evolution reaction catalyst

Laura G. Graversen,[a] Nicolas Schlegel,[a] Freja B. Holde,[a] Adrian S. Arjona,[a] Stefanie Punke,[a] Tobias M. Nielsen,[a] Andy S. Anker,[a] Jonas Forner,[b] Gustav. K. H. Wiberg,[b] Matthias Arenz,[b] Rebecca K. Pittkowski,*[,a] and Kirsten M. Ø. Jensen*[,a]

[a] Department of Chemistry and Nanoscience Center, University of Copenhagen, 2100 Copenhagen Ø, Denmark
[b] Department of Chemistry, Biochemistry and Pharmaceutical Sciences, University of Bern, Freiestrasse 3, Bern, 3012, Switzerland

*Corresponding authors: rebecca.pittkowski@chem.ku.dk and kirsten@chem.ku.dk

Abstract
Iridium oxide nanoparticles are efficient catalysts for the acidic oxygen evolution reaction (OER). We present a straightforward one-pot hydrothermal synthesis method to produce sub-1 nm Ir oxide nanoparticles in a single step, with size control achieved through post-synthesis annealing. By combining X-ray total scattering and pair distribution function (PDF) analysis with small-angle X-ray scattering (SAXS), we find that the sub-nanometer-sized oxide has an increased number of edge-sharing [IrO_6]-octahedra compared to the thermodynamically favorable rutile structure. PDF modelling using various cluster motifs reveals that a sheet-like cluster, derived from rutile and comprising seven [IrO_6]-octahedra with a (110)-exposed surface, can describe the increased Ir-Ir edge-sharing connectivity. We further find that cluster growth leads to a decrease in the number of edge-sharing motifs, going towards the bulk rutile structure upon annealing. *Operando* X-ray total scattering and PDF analysis during OER reveal high structural stability of the ultra-small (<3 nm) Ir oxides.

Introduction
Shifting towards a hydrogen-based economy to address the current energy crisis depends on developing efficient technologies for water electrolysis. In this regard, polymer exchange membrane (PEM) electrolyzers operating in acidic environments are a promising solution, operating at high current densities, high pressures, with a low gas cross-over, and a compact system design.[1, 2] However, at the anode of PEM electrolyzers, the oxygen evolution reaction (OER) suffers from slow kinetics, acting as the bottleneck reaction, requiring large overpotentials to achieve the desired current densities.[3] In addition, the harsh conditions in which PEM electrolyzers operate limit the type of catalyst that can be used. Iridium oxide-based catalysts remain the definitive choice for activity and high stability.[4-6] However, iridium is scarce and expensive. At typical loadings of 1-2 mg cm^{-2} for large-scale iridium-based electrolysers[7], upscaling to a terawatt energy scale would exceed the planet's Ir reserves.[8] To address this, achieving a high dispersion of iridium to maximize the surface-to-mass ratio is critical for its effective use as a catalyst. One strategy involves synthesizing ultra-small nanoparticles (<3 nm).[9, 10] Wet-chemical methods have been widely explored for IrO_2 nanoparticle fabrication, and numerous routes have been reported.[11] Most approaches, however, proceed through multi-step pathways in which an intermediate phase is first formed. These syntheses typically start from simple iridium salts such as $IrCl_3$ or iridates M_2IrCl_6 (M = H, Na, NH_4). Through different synthesis steps, a wide range of different intermediates have been reported, including metallic Ir colloids,[12] aqua/hydroxide/chloro-iridate complexes,[13-15] iridium nitrates,[16] and hydrous Ir(oxy)hydroxides formed by alkaline hydrolysis of H_2IrCl_6.[13, 17] Many of the reported Ir(oxy)hydroxides arise from variations of the Bestaoui hydrothermal route,[18] involving slow hydrolysis of $IrCl_3$ over 13 hours, followed by hydrothermal treatment producing amorphous Ir(III/IV) oxides.[19] Regardless of the specific route, these intermediates are subsequently either thermally converted to IrO_2[11, 19, 20] or electrochemically converted to "hydrous" or "amorphous" IrO_x.[13, 21] While these poorly crystalline counterparts are reported to be more catalytically active than crystalline IrO_2, they suffer from instability.[7, 22-24] As a result, direct wet-chemical routes to anhydrous, stable IrO_2 remain highly sought after.[11] Hydrothermal methods using simple Ir salts in alkaline

View Article Online
DOI: 10.1039/D6TA02189A

solution have similarly tendency to produce Ir hydroxides rather than anhydrous IrO_2.[25, 26] Attempts to overcome this limitation by introducing strong oxidants (e.g., H_2O_2 or Na_2O_2) instead lead to the formation of complex iridate oxides such as pyrochlores.[26, 27] Interestingly, rutile crystallization can be enabled by introducing a dopant metal precursor that also acts as the oxidant; for example, $HRuO_4$ which promotes the formation of mixed rutile $Ir_{1-x}Ru_xO_2$.[28] Collectively, these studies highlight a key gap in the field: a robust, one-step wet-chemical synthesis method for nanocrystalline IrO_2.

It is well established that size, structural motif, Ir coordination, and oxidation state[29] of Ir oxide significantly influences its electrocatalytic activity and stability.[30-32] Nevertheless, the structure of ultra-small Ir oxide catalysts is often assumed to be rutile as bulk IrO_2.[33-35] This is due to the small nanocrystal size, which makes it challenging to fully characterize the catalyst's atomic structure using conventional methods: in powder X-ray diffraction (PXRD), the small crystals lead to broad and diffuse peaks, which are difficult to analyze.[36] Instead, pair distribution function (PDF) analysis of X-ray total scattering data can offer atomic-scale structural insights on ultra-small,[36-38] amorphous,[39-42] or disordered[43, 44] materials that only exhibit local order. For example, PDF has been used for analyzing the structure of amorphous IrO_x, linking the presence of hollandite-like domains to enhanced catalytic activity.[45-47] PDF has also recently been used to investigate catalyst structures under *operando* conditions during OER. Pittkowski *et al*. used *operando* X-ray total scattering with PDF combined with small-angle X-ray scattering (SAXS) to elucidate the active iridium oxide phase forming from electrochemically oxidized sub-3 nm Ir nanoparticles.[48] By correlating particle size information from SAXS with local domain size insights from PDF, they identified ordered < 1 nm Ir oxide domains within larger disordered particles. However, it is unclear if such structures also appear if the as-synthesized particles are oxides rather than metallic Ir nanoparticles.

Here, we present a one-step hydrothermal synthesis method for the preparation of IrO_x clusters smaller than 1 nm. Our direct hydrothermal synthesis circumvents the need for an initial hydrolysis step. We furthermore demonstrate precise control of particle sizes through post-synthesis annealing at different temperatures. The as-synthesized particles and the structural changes induced by annealing are analyzed using PDF, SAXS, and transmission electron microscopy (TEM). Our data show that hydrothermal treatment produces sub-1 nm rutile-like IrO_x clusters predominantly grown along the (110)-plane. Upon annealing, these clusters undergo structural changes, forming rutile-structured spherical particles (2-3 nm) at 450 °C that preferentially grow along the crystallographic c-direction into elongated nanorods at 500 °C.

To understand the changes in the atomic structure during the activation of the IrO_x nanoparticles under acidic OER conditions, we use *operando* X-ray total scattering.[49] Unlike the significant structural disordering observed in electrochemically oxidized Ir,[48] we find that as-synthesized IrO_x is structurally robust, only undergoing minor irreversible oxidation upon electrocatalytic activation. The rutile motifs in ultra-small IrO_x catalysts are structurally stable during operation, and do not form the same disordered oxide motif as seen when oxidizing metallic Ir nanoparticles for the OER. Our findings emphasize the importance of thorough structural characterization of electrocatalysts under operating conditions to fully understand their structure-performance relationships.

Results and Discussion

Synthesis and structure characterization of IrO_x nanoparticles

We first synthesized ultra-small iridium oxide nanoparticles (<1 nm) hydrothermally. Our simple, one-pot, surfactant-free synthesis is described in detail in the Methods section. Briefly, it involves dissolving H_2IrCl_6 and NaOH in deionized water. The solution is then hydrothermally treated in an autoclave at 150 °C for 4 hours. Subsequently, the as-synthesized dried powders were annealed at 400, 450, or 500 °C for 1 hour.

Transmission electron micrographs of the annealed samples are shown in Figure 1. Agglomeration of small particles is observed in all images, which is characteristic of unsupported nanoparticles. In the 400 °C sample (Figure 1a), spherical particles with sizes of 1-2 nm are observed. High-resolution TEM (HRTEM) images reveal lattice fringes, indicating the presence of crystalline domains. The d-spacings extracted from Inverse Fast Fourier Transform (IFFT) analysis of randomly selected crystallites reveal multiple orientations within the sample, which can be indexed to the (110) and (101) crystallographic planes of the rutile crystal

View Article Online
DOI: 10.1039/D6TA02189A

structure. Details on the IFFT analysis are provided in Figure S1. The 450 °C sample (Figure 1b) shows a broader distribution of crystallite sizes, although the particles largely retain a spherical morphology (examples highlighted in yellow). In contrast, the 500 °C sample (Figure 1c) exhibits elongated rod-like morphologies (yellow highlights), consistent with particle growth during annealing. However, extensive agglomeration hinders the analysis, preventing determination of mean particle sizes.

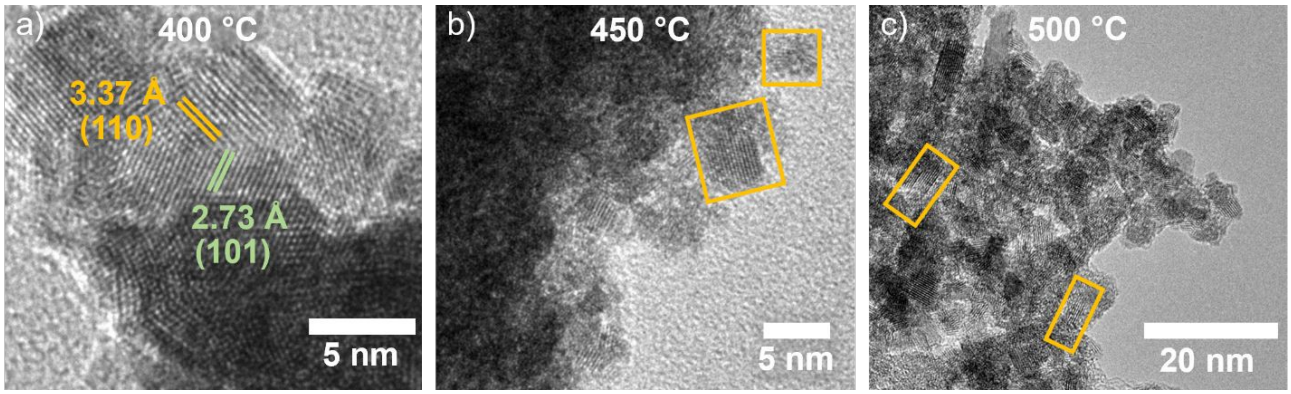

Figure 1. TEM micrographs and d-spacings obtained from IFFT analyses of hydrothermally synthesized IrO_x after annealing. a) 400 °C, b) 450 °C, and c) 500 °C samples.

The trends observed in TEM are corroborated by powder diffraction data of the four synthesized samples shown in Figure 2a alongside a calculated diffraction pattern of rutile IrO_2. Bragg peaks corresponding to rutile IrO_2 are present after annealing at 450 °C and 500 °C. However, the 500 °C PXRD exhibits a (101)-reflection (at 2.4 $Å^{-1}$) that is more intense than expected relative to the (110)-reflection (at 2.0 $Å^{-1}$), suggesting anisotropic growth. This is supported by Rietveld refinements, where an anisotropic particle shape model is required (SI Figure S2) to fit the peak intensities, yielding rod-like rutile crystallites with an approximate width of 3 nm and a length of 4-5 nm. Comparatively broader Bragg peaks are exhibited for the 450 °C analogue, indicating smaller crystallite sizes and inhibiting Rietveld analysis. In contrast, the 400 °C and pristine samples display significantly broader peaks dominated by diffuse scattering, suggesting less crystalline structures or smaller crystallites. However, the positions of the broad features align with the peaks observed in the more crystalline samples, indicating the formation of rutile-like Ir oxide (IrO_x).

The broad Bragg peaks prevent detailed structural insights from PXRD. Instead, PDF analysis of X-ray total scattering data can be used to extract structural information by presenting the real-space atomic pair correlations. The corresponding PDFs of the samples are shown in Figure 2b. The PDF peaks observed in the local region agree with iridium oxide, as observed in the comparison with a simulated PDF from bulk IrO_2 rutile (Figure S3a). Information on the crystallite sizes is contained in the extent of atomic correlations. From the insert in Figure 2b and Figure S3b, these are estimated to be ca. 8, 10, 25, and 50 Å for the pristine, 400, 450, and 500 °C samples, respectively. At first glance, the PDFs thus show hydrothermal formation of extremely small or disordered particles, whose structure is related to that of bulk, rutile IrO_2. The data furthermore show increasing long-range order with higher annealing temperatures. Examining the low-*r* region of the PDFs in Figure 2b, the first Ir-O peak appears at ca. 2.0 Å, while the peaks at 3.1 Å and 3.6 Å represent Ir-Ir pairs from edge-sharing (ES) and corner-sharing (CS) [IrO_6]-octahedra, respectively. The intensity of the 2.0 Å (Ir-O) and 3.1 Å (ES) peaks remains similar across samples. In contrast, the 3.6 Å peak intensity (CS) increases significantly for the 450 °C and 500 °C samples, indicating annealing-induced structural changes.

View Article Online
DOI: 10.1039/D6TA02189A

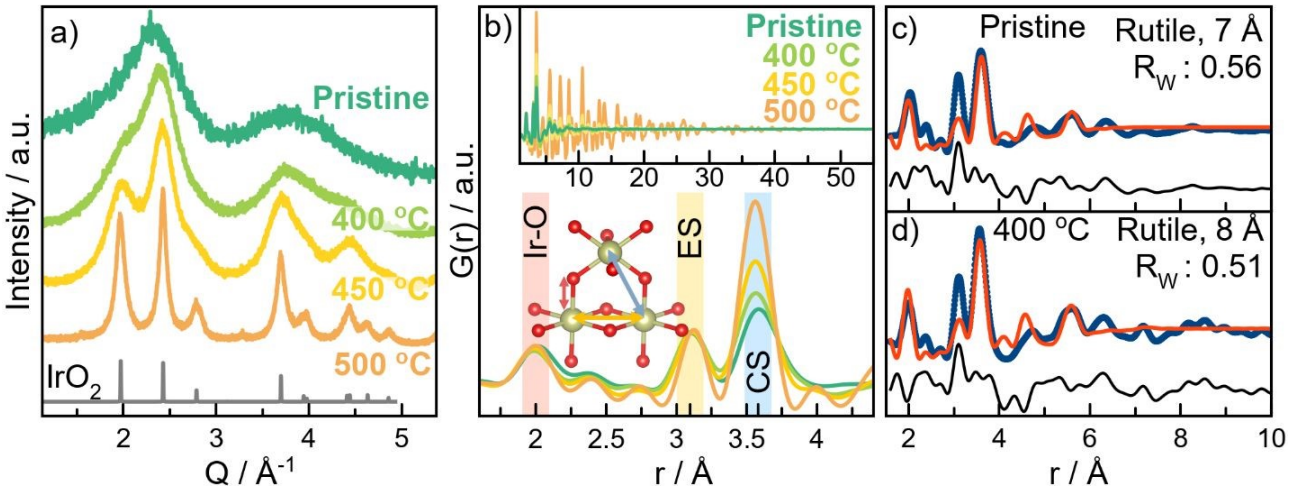

Figure 2. Diffraction data of hydrothermally synthesized IrO_x Pristine, and subsequently annealed at 400 °C, 450 °C, or 500 °C. a) PXRD patterns of the four samples with a calculated pattern of rutile IrO_2 in grey. b) PDFs of the local *r*-range, full-range PDFs shown in the inset. PDF fits using rutile IrO_2 as the structural model to the c) Pristine sample and d) 400 °C sample.

ES-rich clusters from hydrothermal synthesis and 400 °C annealing

To gain further structural insights into the synthesized structures, we model the PDFs. We begin by investigating the as-synthesized pristine and 400 °C annealed samples. As the peak positions in PXRD (Figure 2a) generally align with the rutile structure, we first use this as the structural model in PDF refinements (Figure 2c-d). We use a spherical envelope function to describe the size and shape of the particles. The model gives a reasonable fit to the PDF peak positions, and nanoparticle sizes of 7-8 Å are obtained. However, while the Ir-O peak at 2.0 Å and the CS Ir-Ir peak at 3.6 Å are well described, the ES Ir-Ir peak at 3.1 Å is much less intense in the rutile model compared to the PDFs of the pristine and 400 °C samples. To identify the source of the increased ES Ir-Ir in the pristine and 400 °C samples, we look for other known iridium oxide and hydroxide structures. The hollandite structure[50] consists of [IrO_6]-octahedra arranged to form 2x1 cavities (see Figure 3a) and has been reported by Willinger *et al*. to exist as the active species in iridium hydroxide OER catalysts.[47] Fits to the pristine and 400 °C PDFs using the hollandite structure and the resulting refined structure are shown in Figure S4. As shown in Figure S3-S4, a much larger ES/CS peak-intensity ratio is exhibited by the hollandite structure than observed in our data. Achieving an ES/CS-ratio that describes the data requires a large reduction of the β angle (fit parameters reported in Table S1). In turn, this elongates the Ir-O bonds to unphysical lengths (~2.3 Å), far exceeding the longest reported Ir^{4+}-O lengths (2.096 Å).[51] This demonstrates that the structure of the pristine and 400 °C samples cannot be properly described by hollandite. We also compared the experimental PDF with that calculated from iridium oxyhydoxide (IrOOH, Figure S3), which does not agree with the experimental PDF.

We therefore proceeded to calculate PDFs for various, discrete sub-1 nm motifs cut out from the rutile structure. The models and PDFs are shown in Figure 3b-f and 3g, respectively, where they are also compared to rutile and hollandite. Model 1 represents a spherical cutout of the rutile structure. This model thus contains all aspects of the rutile structure with the center atom chosen as the center of the unit cell, i.e., the Ir atom at (0.5, 0.5, 0.5). When fitting this structure to the PDF, we found that it, as the bulk rutile model, describes the position of the peaks, but not the correct intensity ratio. The intensity of the edge-sharing Ir-Ir peak is especially lower than in the data, as illustrated in Figure 3h, where the ratios from the models have been calculated and plotted. The figure also includes ratios obtained from the experimental PDFs. Model 2 is similar to Model 1 but is extended along *c* to introduce a larger amount of edge-sharing octahedra. However, while the ES/CS intensity ratio gets closer to that of the experimental data, the medium range order peak intensities do not agree with the data.

View Article Online
DOI: 10.1039/D6TA02189A

We therefore cut out other motifs, and look towards those represented in specific crystallographic planes in the rutile structure. The (100) plane only contains edge-sharing octahedra, while the (001) plane has edge-sharing octahedra in a zig-zag pattern along *c*. As the PDF clearly shows both edge-sharing and corner sharing, we must include both motifs in the model. We therefore considered the 110 plane, which is the most thermodynamically stable surface in the rutile structure.[52, 53] Models 3, 4, and 5 are all cut from this layer, but differ in their size. PDF refinements of the pristine and 400 °C samples using these motifs as structural models are shown and discussed in SI Figure S5. Based on the goodness-of-fit (R_W-value), Models 3 and 4 provide equally good descriptions of the pristine (Figure 4a-b) and 400 °C (Figure 4c-d) PDFs. Although the R_W-values are comparable, model 3's ES/CS ratio matches that of the pristine and 400 °C samples better (Figure 3h), whereas the smaller model 4 has a lower ES/CS ratio. We thus propose that the sub-1 nm Ir oxides are built from [IrO_6]-octahedra linked through edge- and corner-sharing, primarily exposing the most stable surface, corresponding to the (110) plane in the rutile structure.[53]

We note that the models only describe the main structural motifs present in the particles, and cannot provide information on the exact surface coordination, solvation, etc. Most likely, clusters of slightly different sizes and shapes are present in the sample.

View Article Online
DOI: 10.1039/D6TA02189A

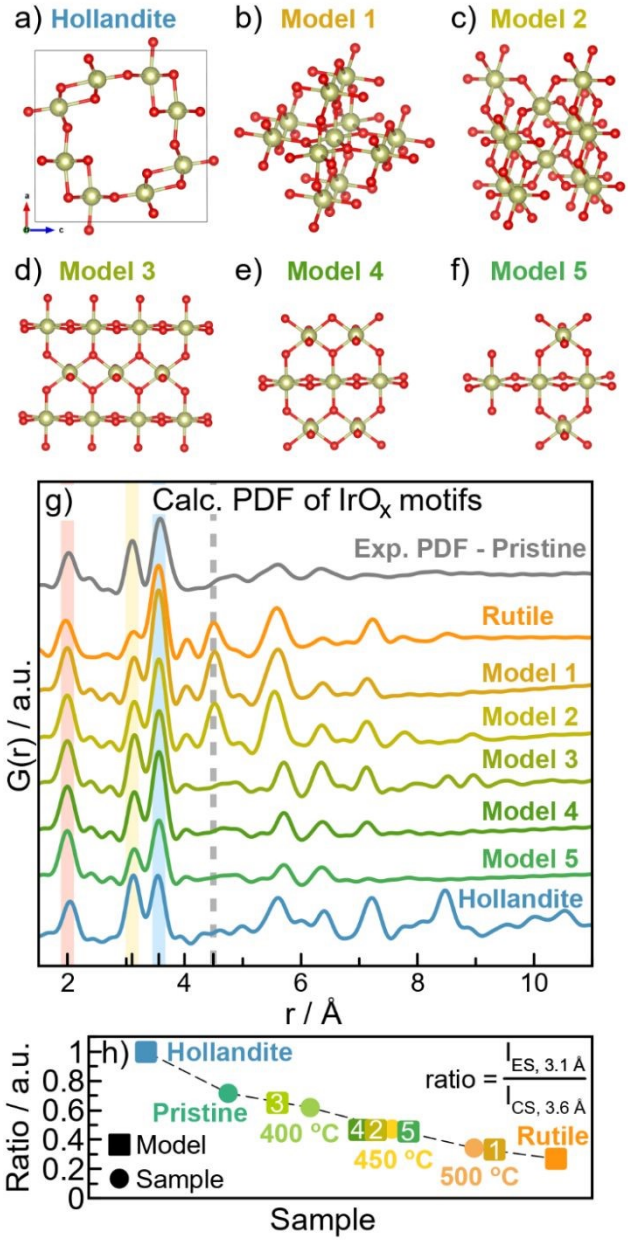

Figure 3. a) Hollandite structure with 2x1 cavities. b-f) Different cut-outs from the rutile structure. g) Calculated PDFs of various Ir oxide motifs, with the experimental PDF of the Pristine sample for reference. h) Ratio of the measured PDF peak intensity of the ES peak at 3.1 Å to the CS peak at 3.6 Å (circles), including ratios obtained from the calculated PDFs in g) (square).

View Article Online
DOI: 10.1039/D6TA02189A

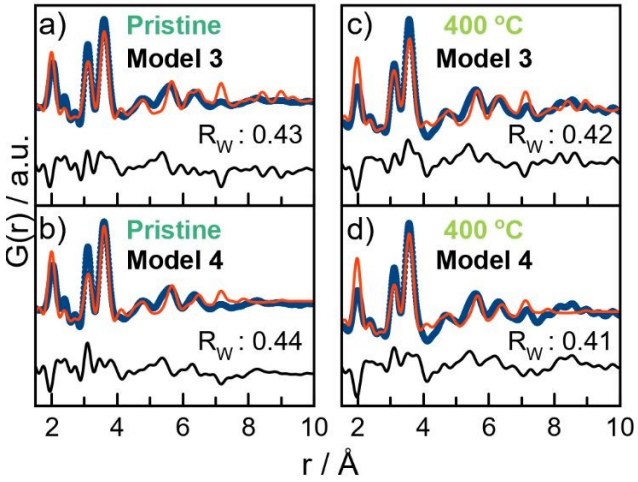

Figure 4. PDF fits for the Pristine and 400 °C samples using two cluster models. a) Pristine sample fitted with Model 3 (corresponding to Figure 3d). b) Pristine sample fitted with Model 4 (Figure 3e). c) 400 °C sample fitted with Model 3. d) 400 °C sample fitted with Model 4.

Extended rutile crystallization induced by high-temperature annealing

Turning to the 450 °C sample, the PDF correlation lengths exceed the size of the cluster, which indicates that an extended crystallization has occurred. Therefore, we use rutile as the structural model. As shown in Figure 5a, by employing a spherical envelope function describing the crystallite size, the rutile model effectively captures the peak positions. However, issues in accurately capturing the peak intensities lead to the observed feature-rich difference curve. Noticeably, these features resemble the calculated PDF of the Model 3 cluster (structure shown in Figure 3d). This indicates the presence of a large distribution of particle sizes, consistent with the TEM analysis (Figure 1b). To address this, we include the sub-1 nm cluster model (Model 3) in the refinement, which substantially improves in both the local (grey highlight) and global (>20 Å) fit range (Figure 5b). PDF refinements reveal a mass ratio of ~36% cluster and 64% 3 nm rutile, suggesting that annealing at 450 °C for 1 hour predominantly grows the sub-1 nm clusters into ca. 3 nm spherical IrO_2. The difference curve still shows significant features, including a misfit of the Ir-O peak, which reflects limitations of the simple two-phase model in representing the size distribution.

Lastly, we examine the 500 °C sample. Figure 5c shows a fit using the crystalline rutile model, where a spherical envelope function is again used to describe the crystallite size. The model fits well for PDF features below 20 Å, showing formation of a rutile structure, in agreement with the PXRD. However, the long-range order (r >20 Å) is poorly described by the spherical shape function. To reflect the anisotropic morphology suggested by TEM and PXRD, a spheroidal shape factor was implemented in the PDF refinement of the 500 °C sample. With this adjustment, the features above 20 Å are captured properly (Figure 5d), estimating a rod length of ca. 7 nm and a width of 1 nm. The spheroidal model may overfit noise at high *r*-values, potentially overestimating the crystallite size, explaining deviations from PXRD results. TEM further supports rod formation and reveals a distribution of crystallite sizes (Figure 1d). IFFT analysis of three randomly selected rods (yellow highlighted regions in Figure 5e) shows consistent d-spacings of ~3.3 Å, corresponding to the (110)-crystallographic plane of the rutile structure.[54] The random deposition of nanoparticles onto the TEM grids during drop-casting should ensure random rod orientations. The absence of d-spacings for the (101)-plane (~2.7 Å) suggests preferential growth along the crystallographic c-direction. Further details on the IFFT analysis are provided in Figure S1.

View Article Online
DOI: 10.1039/D6TA02189A

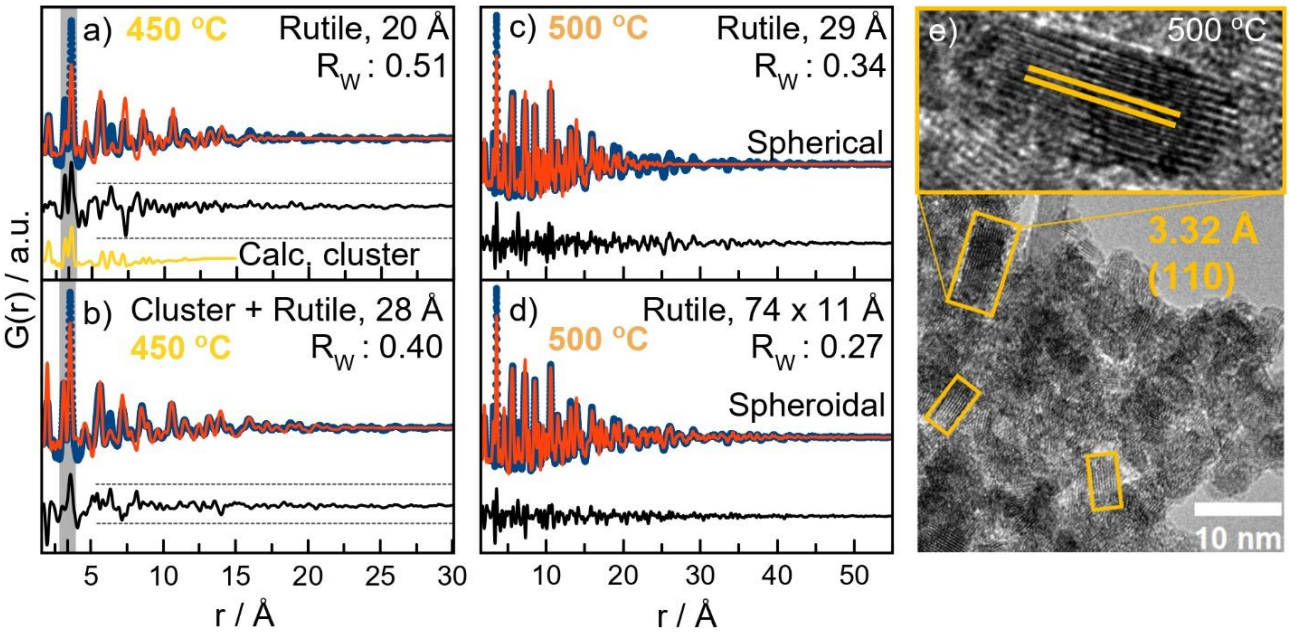

Figure 5. PDF fits using rutile IrO_2 as the structural model. a) 450 °C sample fitted with a monodisperse spherical model. Notice the resemblance of the difference curve with the calculated PDF (yellow) of a sheet-like cluster (Model 3) cut along the (110)-plane of the rutile structure. b) Fit with the Model 3 cluster along with a 28 Å spherical rutile model. The grey-highlighted region shows local improvements, while narrowing the difference curve above 6 Å indicates global improvements from the monodisperse model. c) 500 °C sample fitted with a spherical nanoparticle model, and d) fitted with a spheroidal shape model. e) TEM image showing elongated rods formed at 500 °C.

PXRD and PDF analyses thus indicate formation of ultra-small domains. To confirm whether the smallest samples (pristine and 400 °C) consist of ultra-small crystalline particles or if their diffuse scattering and low coherence length are due to an amorphous structure, SAXS was performed. Additionally, SAXS was used to further examine the morphology of the larger samples (450 °C and 500 °C). The data are shown in Figure S6. Modelling of the SAXS data (described in detail in Table S2) revealed spherical diameters of ~1 nm for both the pristine and 400 °C samples and 2 nm for the 450 °C sample. These values align closely with the cluster and crystallite sizes obtained from PDF analysis (Table 1), indicating that the correlation sizes in the PDF correspond to individual particles. For the 500 °C sample, SAXS supports a cylindrical morphology (Figure S6f in SI). The analysis suggests average nanorod diameters of 5 nm and lengths of 15 nm. This finding is consistent with TEM (Figure 5e), suggesting that TEM's localized images represent the sample's average morphology. The larger sizes from SAXS, compared to PXRD and PDF, could indicate multiple crystallite domains within the rod particles or agglomerated rods. However, as discussed in Figure S6, we could not reliably model polydispersity from the present data.

An overview of the structure, sizes, and morphologies of the four samples is provided in Table 1, highlighting the presence of size-dependent atomic structures in ultra-small IrO_x nanoparticles. This structural analysis suggests that hydrothermally synthesized sub-1 nm IrO_x are characterized by sheet-like structures with exposed (110)-facets from the tetragonal rutile structure. The samples cannot be described using the hollandate structure which would be expected for (oxy)hydroxides rather than oxides. Minimal structural changes or growth take place upon annealing at 400 °C. This observation contrasts with previous reports that associate increased ES/CS ratios with local monoclinic or orthorhombic distortions.[31, 55] When the annealing temperature increased to 450 °C, isotropic growth transforms some of these sheets into ~3 nm spherical rutile IrO_2, as graphically shown in Figure 6. Eventually, increased temperatures promote

View Article Online
DOI: 10.1039/D6TA02189A

anisotropic growth, possibly driven by the preferential exposure of the thermodynamically stable (110)-surface,[52, 53] resulting in the formation of nanorods.

Table 1. Overview of the obtained particle size, morphology, and structure of the four samples from SAXS and PDF.

Sample	Size SAXS	Size PDF	Shape SAXS	Shape PDF	Structure
Pristine	12 Å	7 Å	Spherical	Spherical	Cluster
400 °C	12 Å	8 Å	Spherical	Spherical	Cluster
450 °C	22 Å	8 + 28 Å (polydisperse)	Spherical	Spherical (polydisperse)	Cluster + rutile
500 °C	50x130 Å	11x74 Å	Rod	Rod	Rutile

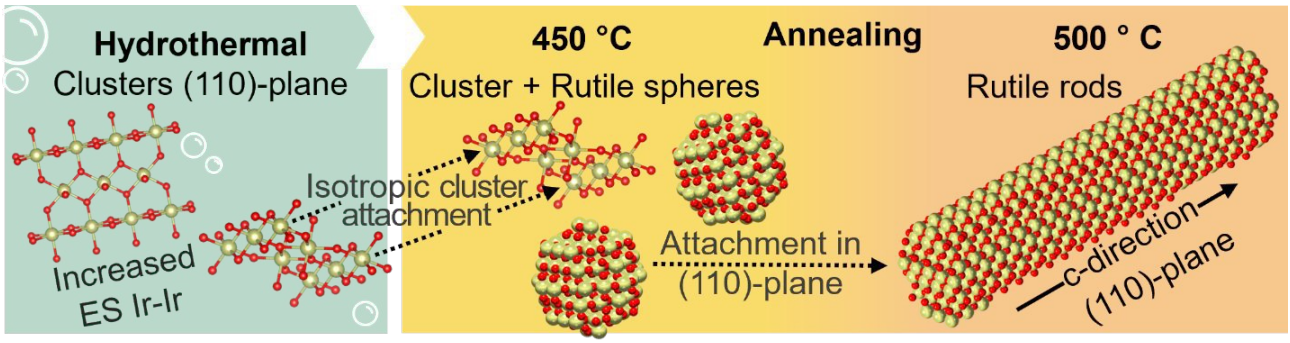

Figure 6. Schematic of the proposed growth pathway. Annealing at 450 °C promotes hydrothermally synthesized IrO_x clusters to stack forming spherical rutile IrO_2 nanoparticles, which at higher temperatures attach preferentially along the *c*-axis forming elongated rutile nanorods.

Structural changes during OER

Having gained a thorough understanding of the structure of the synthesized samples, we move on to investigate how the particles behave and change under OER conditions. Therefore, the annealed IrO_x nanoparticles (400 °C, 450 °C, and 500 °C) were tested in an *operando* gas diffusion electrode (GDE) setup, illustrated in SI Figure S7.[49] These experiments allow studying of the catalyst structure under operating conditions.

Catalyst usage requires depositing the particles on carbon. PDFs of the as-synthesized IrO_x and the carbon-supported IrO_x measured in the *operando* setup are provided in Figure S8. We find the PDFs of the 500 °C sample to remain largely unchanged before and after carbon deposition. In contrast, for the 400 °C and 450 °C samples, the intensity of the Ir-Ir CS peak (3.6 Å) appears to have decreased after carbon deposition. While this could imply minor structural changes during the electrode preparation process, it is more likely to originate from challenges in background subtraction of the *operando* data, as discussed in SI Figure S9 and shown by Pittkowski *et al*.[48]

X-ray total scattering data for PDF analysis were collected at OER conditions, running a chronoamperometric protocol. The catalysts were stepped from open circuit potential (OCP, see SI Table S3) to 1.4 V_{RHE} in intervals of 0.2 V and then to 1.6 V_{RHE} at intervals of 0.1 V, after which the potential program was reversed back to 1.0 V_{RHE}. Each potential step was held for 20 min. The three samples' current responses in the operando setup, normalized to the geometric area, together with *ex situ* polarization curves

View Article Online
DOI: 10.1039/D6TA02189A

are shown in Figure S10.The *operando* measurements show an inverse correlation between the samples' particle sizes and the current response, with the 500 °C sample exhibiting the highest current density. This is contrary to the expected trend, as samples containing smaller particles generally exhibit larger electrochemically accessible surface areas, resulting in increased current responses. However, because the catalysts are deposited on a carbon support and further vacuum filtrated on a microporous layer, we cannot use capacitance as a proxy for electrochemically accessible surface area. Consequently, variations arising from catalyst-layer deposition and morphology cannot be excluded as the origin of the observed current trends. The *ex situ* measurements (Figure S10b) corroborate this interpretation, as we find the sample with the smallest crystallite size to exhibit the largest mass activity. Therefore, we focus the discussion on the structural stability of the catalysts rather than their intrinsic activities.

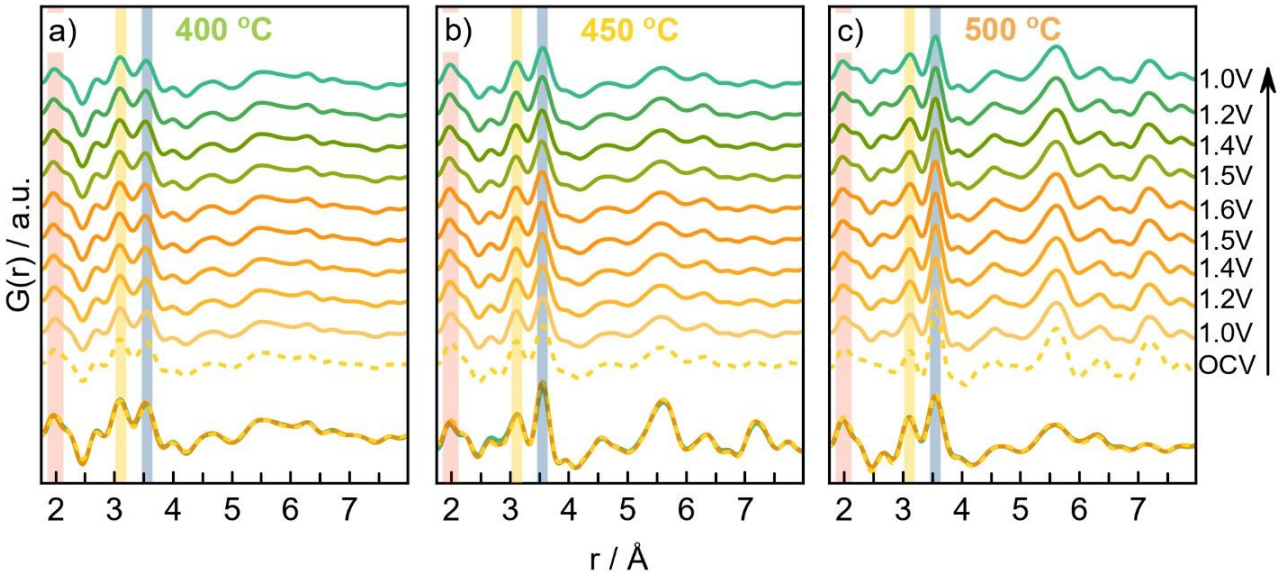

Figure 7. *Operando* chronoamperometry protocol stepping from OCP to 1.6 V_{RHE} and back to 1.0 V_{RHE}. Simultaneously measured PDFs for the a) 400 °C sample, b) 450 °C sample, and c) 500 °C sample.

To investigate how the as-synthesized catalyst structure changes during OER, we look at the *operando* PDF data (Figure 7) at every potential step. Across the applied potential range, no major changes in the maximum correlation length are observed (see Figure S11), indicating that the cluster and crystallite sizes remain stable throughout the OER protocol for all three samples. To investigate local structural changes, we analyze the Ir-O peak (red highlight), Ir-Ir ES peak (yellow highlight), and Ir-Ir CS peak (blue highlight). As explained in detail in Figure S12, we applied Gaussian fitting to each of the three peaks, tracking the peak position throughout the electrocatalytic process. The fitted peak positions are shown in Figure 8 as a function of applied potential. Here, we observe a shift of the Ir-O peak towards smaller *r*-values at more oxidative potentials, indicating an Ir-O bond contraction. This observation is consistent with Ir oxidation as is expected under OER conditions from previous *operando* spectroscopy studies of iridium oxide based materials.[6, 29, 56, 57] Combining PDF with *operando* X-ray absorption spectroscopy, Pittkowski *et al.*[48] demonstrated that the Ir-O bond length extracted from PDF can be used as a quantitative proxy for the Ir oxidation state. Based on this correlation, they proposed the presence of an Ir^{5+} active species at oxidizing potentials. In our data, the shortened Ir-O distances of 1.94-1.95 Å at high potentials are consistent with the formation of such Ir^{5+} species, in agreement with previous studies by Diklic *et al.*[29] and Lebedev *et al.*[58] Additionally, Minguzzi *et al.*[59] demonstrated the involvement of an Ir^{5+} intermediate in Ir/IrO_2 core-shell nanoparticles during OER through *operando* X-ray absorption spectroscopy.

View Article Online
DOI: 10.1039/D6TA02189A

During the reductive potential scan, the Ir-O bond expands again as the reduction takes place; however, it appears that this expansion is not completely reversible (Figure 8a). Such irreversible oxidation has also been observed in electrochemically oxidized Ir nanoparticle catalysts.[60] In contrast to the Ir-O distances, the Ir-Ir correlations show less pronounced responses to the applied potential. In the case of the two small nanoparticles (400 °C, 450 °C), the data indicate a very slight reversible contraction of the Ir-Ir bonds (both ES and CS) during the potential step cycle (Figure 8b-c). We note, however, that the observed changes in peak position are close to the *r*-resolution of the data.

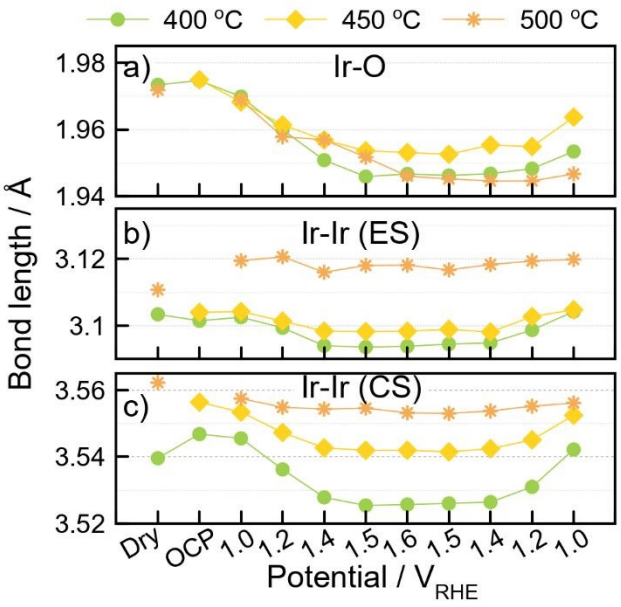

Figure 8. Parameters extracted from Gaussian fitting of *operando* PDF data. a-c) Changes in bond length as a function of potential during the potential step protocol.

Our *operando* analysis thus indicates that all three samples are generally structurally stable under the applied conditions. We observe small changes for the smallest particles, which we relate to oxidation. Possibly, the ultra-small size of the IrO_x clusters allows greater oxidation-driven breathing of the structure than in the crystalline IrO_2 nanoparticles, yet without causing disordering or amorphization. While PDF is a bulk technique, the small crystallite size (sub 1 nm for the 400 °C sample) means that surface atoms make up a large part of the material, and thus contribute significantly to the observed signal.[61, 62] Consequently, our data indicate that no significant surface restructuring[63] to IrO_2OH or amorphisation[64] occurs in these catalysts under OER conditions. The stability of the particles contrasts with the significant structural disordering observed in electrochemically oxidized Ir, as previously investigated with PDF analysis.[48]

The structural robustness is furthermore illustrated when tracking the intensity ratio between the ES (3.1 Å) and CS (3.6 Å) peaks in the *operando* PDFs. As shown in Figure 9a, the largest crystallites (500 °C sample) do not exhibit a change in the ES/CS ratio during the potential step protocol (from OCP to 1.6 V_{RHE} and back to 1.0 V_{RHE}), maintaining a steady ratio throughout. A small change is observed for the two smallest particles (400 °C and 450 °C), as the data show a slight reversible decrease in the ES/CS intensity ratio by ~5% during chronoamperometry stepping. To investigate the structural stability of the catalysts further, we applied a potential of 1.65 V_{RHE} for 2 hours while recording *operando* PDF (current responses seen in Figure S13). Figure S14 shows the local range of the PDF measured at the beginning and after 2 hours of stability testing. Again, minimal structural changes were observed throughout the whole measurement (see Figure S15). The intensities of the ES and CS peaks were again determined through Gaussian fitting (Figure 9b), revealing a very small but systematic and continuous decrease in the ES/CS peak ratio during OER for IrO_x

View Article Online
DOI: 10.1039/D6TA02189A

crystallites below 3 nm (400 °C and 450 °C). This reduction in ES Ir-Ir motifs indicates that the nanoparticles may become structurally more similar to the thermodynamically stable rutile structure during extended OER.[54] Possibly, the decreased amount of ES Ir-Ir may result from preferred Ir dissolution from ES sites within the sheet-like crystallites. In contrast, the 500 °C sample, which closely resembles the ideal rutile structure from the beginning, likely refrains from ES Ir-Ir dissolution (see Figure S14). Apart from these very small changes to the PDF, we find no evidence of dissolution-redeposition-induced reorganization, in contrast to previous reports.[55]

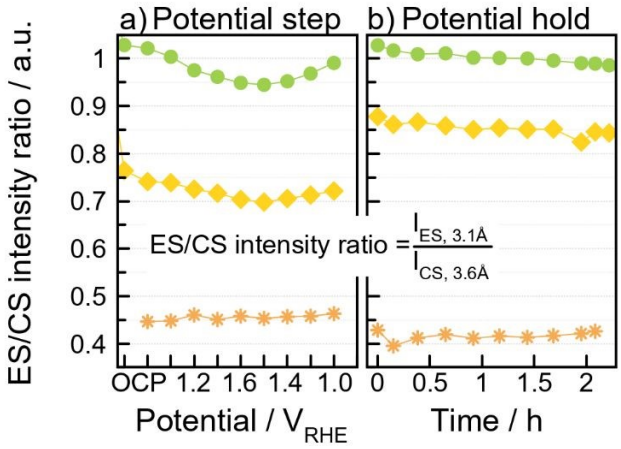

Figure 9. Changes in peak intensity ratio of ES peak at 3.1 Å and CS peak at 3.6 Å extracted from Gaussian fitting of *operando* PDF data recorded during a) potential step protocol, and b) holding a constant potential of 1.65 V_{RHE}.

Surprisingly, the structural stability of the 500 °C sample does not translate into electrochemical stability. The largest crystallites show the greatest current losses, decreasing by 31% and 27%, respectively, after 2 hours (See Figure S13). In contrast, the smallest particles (400 °C sample) are more electrochemically stable, exhibiting only a 16% current loss. While this may seem contradictory, given that the largest crystallites were structurally the most stable as observed in the PDF (see Figure S14), it is important to note that the PDF exclusively probes the structural stability of the Ir oxide catalyst. In contrast, the electrochemical current reflects a combination of phenomena occurring in the gas diffusion cell, including carbon support degradation, mass transport limitations, oxygen accumulation on the catalyst surface, and changes in the electrolyte environment over time.[65] Hence, the loss of activity is more likely linked to catalyst film deterioration than catalyst particle degradation. Figure S16 shows TEM images of the particles that could be recovered from the *operando* experiment. The relatively small nanoparticle size, combined with significant carbon contamination originating from the gas diffusion layer and Nafion binder makes imaging of the particles by (S)TEM challenging. Nevertheless, we observe particles with a rod-like morphology, approximately 10 nm in length and 5 nm in width. These dimensions and morphologies are consistent with those observed for the as-synthesized 500 °C sample. Within the resolution and limitations of the measurements, we therefore do not observe evidence of substantial morphological changes after 2 h under OER operating conditions.

Conclusion

We have successfully synthesized iridium oxide below 1 nm via a one-step hydrothermal method. Using PDF and SAXS analysis, we showed that the structure of the as-synthesized particles deviates substantially from bulk rutile IrO_2, exhibiting an increased amount of edge-sharing [IrO_6]-octahedra. By fitting different discrete models to the PDFs, we suggest that the samples are best described as a sheet of edge- and corner-sharing [IrO_6]-octahedra, demonstrating the PDF's sensitivity to different cluster motifs. Subsequent annealing at different temperatures enables size-tuning of the Ir oxide catalysts. While the structure is

View Article Online
DOI: 10.1039/D6TA02189A

retained when annealing at 400 °C, annealing at 450 °C leads to the formation of polydisperse spherical nanoparticles, ranging from 1 to 3 nm with a rutile IrO_2 structure. Annealing the sample at 500 °C, we find the formation of elongated rods (approx. 5 nm wide and 15 nm long). PDF coupled with TEM analysis shows preferential growth along the crystallographic c-direction.

We further investigated structural changes during electrocatalysis using *operando* PDF. These measurements reveal that the IrO_x nanoparticles exhibit remarkable structural stability. Our measurements show only minor structural changes in the smallest nanoparticles, which we relate to oxidation, as seen primarily from the elongation of the first Ir-O distance. Our data does not indicate any major structural reorganization or amorphization upon catalyst use.

Experimental methods

Synthesis of IrO_x

IrO_x samples were hydrothermally synthesized using 0.04 g (0.1 mmol) of hydrogen hexachloroiridate(IV) hydrate (99.9 % trace metals basis, Sigma-Aldrich) dissolved in 10.0 ml of deionized water in a Teflon-lined steel autoclave to obtain an Ir concentration of 0.01 M. Complete dissolution results in a blue solution. NaOH(s) was added until alkaline conditions (pH ≈ 10) were achieved. The change in pH leads to a color change from blue to yellow. The sealed autoclave was placed in a preheated oven at 150 °C for 4 hours. The precipitates were washed with ethanol (VWR, 96%) three times and left to dry overnight. Subsequent annealing was performed by transferring the dried iridium oxide powder to a porcelain crucible, which was placed in a cold oven. The temperature was increased to 400, 450, or 500 °C at a 30 °C/min ramping rate and maintained at the specified temperature for 1 hour. The sample was annealed in an open crucible, allowing unrestricted exposure to atmospheric air throughout the process.

Total scattering and PDF

Ex situ X-ray total scattering data were measured on the as-synthesized IrO_x powders at DESY on beamline P02.1 using an X-ray wavelength of 0.207345 Å equipped with a Perkin Elmer XRD 1621 flat panel detector.[66] The as-synthesized powders were loaded into Kapton tubes with an inner diameter of 1.0 mm. The X-ray exposure time was 4 min. The obtained data were integrated using PyFAI in Dioptas[67] and background subtracted, normalized and Fourier transformed to PDFs using PDFgetX3[68] with Q_{min} = 0.4 $Å^{-1}$, Q_{max} = 21 $Å^{-1}$, r_{poly} = 0.9 Å, and Q_{damp} = 0.029 $Å^{-1}$. Subsequent modelling was performed using the Diffpy-CMI software.[69]

SAXS

Ex situ SAXS measurements were performed in-house with a Nano-inXider instrument with a wavelength of 1.54 Å. The IrO_x nanoparticles were dispersed in a mix of 3:1 H_2O:IPA and loaded into 1.5 mm borosilicate capillaries. Each sample was measured for 2400 s with a Q-range of 0.006 - 4 $Å^{-1}$. The data were merged, corrected for the background of the solvent and the capillary, and eventually log-binned. The analysis was conducted with SasView 5.0.6.

TEM

TEM micrographs were acquired using a Thermo Fisher Talos 200i TEM operated at a 200 kV acceleration voltage. As-prepared samples were dispersed in HPLC-grade ethanol by ultrasonication with a horn sonicator. 5 µL of the suspension was drop-cast onto Agar Scientific holey carbon film supported on 400-mesh copper grids and air-dried. During imaging, the grids were mounted in a single-tilt FEI ST holder.

Total scattering operando OER on GDE

The catalyst inks for *operando* measurements were prepared by dispersing 0.0079 g IrO_x powder (400, 450, or 500 °C sample) in 2 ml isopropanol (99.8 %, Sigma-Aldrich) and 6 ml ultra-pure water (MilliQ system,

View Article Online
DOI: 10.1039/D6TA02189A

18.2 MΩ, 3 ppb TOC). 32 µl Nafion™ 117 (5 wt% in H_2O, Sigma-Aldrich) was added, and the stock solution was homogenized using a horn sonicator for 4 hours (Qsonica sonicator, Q500). The inks were cooled in ice baths during sonication to prevent solvent evaporation. The stock solutions were diluted to obtain a concentration of 200 $\mu g_{Ir}/cm^2$ by adding 6 ml ultra-pure water and 9 ml absolute ethanol (99.5 %, Sigma-Aldrich) to 2.33 ml stock solution. The resulting ink was horn-sonicated until a homogeneous ink solution was obtained. Over the course of approx. 5 hours, the catalyst inks were vacuum filtrated onto a gas diffusion layer (GDL) with a C-based microporous layer (MPL) coating (Freudenberg H23C8, FuelCell Store). Using a custom-made stencil, the prepared catalyst films were cut into shapes that fit the electrochemical cell. These cuts served as working electrodes (WE) in the three-electrode electrochemical cell developed by Wiberg *et. al.*[49] A platinum mesh served as counter electrode (CE), and a leakless Ag|AgCl (eDAQ) electrode served as reference (RE). 0.5 M perchloric acid (99.999 % purity, Merck) was used as electrolyte. After each experiment, the shift of the RE versus a freshly prepared trapped hydrogen electrode was measured to convert the WE potential to an RHE scale.

X-ray total scattering data were collected on beamline 15-1 at Diamond Light Source using an X-ray wavelength of 0.16167 Å equipped with a Perkin Elmer XRD 4343 CT detector. The obtained data were integrated using PyFAI in Dioptas[67] and Fourier transformed to PDFs using PDFgetX3[68] with Q_{min} = 1.8 $Å^{-1}$, Q_{max} = 20 $Å^{-1}$, and r_{poly} = 0.9 Å. Two *operando* electrochemical protocols were performed. Potential steps from open circuit potential (OCP) were held at 1.0, 1.2, 1.4, 1.5, and 1.6 V vs RHE, followed by stepping back to 1.0 V vs. RHE at the same increments, holding each potential for 20 min. The X-ray beam with a 20 µm vertical size alternatingly probed the active catalyst layer and the carbon support for 10 minutes each. Scattering data on the empty cell and liquid electrolyte were also obtained to allow for background subtraction by linear interpolation between the four sets of scattering data. Catalyst stability was investigated through constant potential holds at 1.65 V vs RHE for 2 hours. Scattering data of the catalyst layer and carbon support were alternately measured every 1 minute, with background subtraction performed similarly to the potential step measurements.

Ex situ electrochemical measurements

Catalyst inks were prepared by dispersing the IrO_x samples in a 3:1 mixture of ultra-pure water (MilliQ system, 18.2 MΩ, 3 ppb TOC) and 2-propanol (99.8 %, Sigma-Aldrich). 0.096 % Nafion ionomer (5 wt.% in aliphatic alcohols, Sigma-Aldrich) were added to the ink, yielding an IrO_x concentration of 1.572 mg mL^{-1}. The inks were dispersed using a horn sonicator (Q500, Qsonica) for 30 minutes while cooling the ink in an ice bath to prevent solvent evaporation. The inks were then drop cast onto printed circuit board electrodes (PCB) to yield mass loading of 20 µg cm^{-2}. The PCBs were prepared following the procedure introduced by Forner et al using the same 3D-printed cell design.[70] Briefly, the as-received PCBs are degreased in 2-propanol and subsequently electroplated first with Pd and then with Au. This provides an acid-resistant substrate and ensures good electrical conductivity between the ink and the substrate. Two glassy carbon rods served as counter electrodes and a freshly prepared trapped hydrogen bubble served as a reversible hydrogen electrode (RHE). Each PCB consists of 8 individual electrodes, one of which is left blank and the others are used electrochemical characterization. 10 consecutive cyclic voltammograms were recorded in 0.5 M H_2SO_4 (prepared from 96 % ultra-pure, Sigma-Aldrich) between 1.25 V_{RHE} and 1.65 V_{RHE} at 0.01 V s^{-1}. The data was collected using a ECi-210 potentiostat controlled by EC4™DAQ software (both Nordic Electrochemistry ApS). The solution resistance was determined *on-line* by applying an AC perturbation of 5000 Hz with an amplitude of 10 mV. The data was *iR* corrected using the determined solution resistance. Capacitive contributions were removed by averaging forward and backward scan. Possible current offsets were removed by subtracting the currents recorded at 1.28 V_{RHE} from the whole CV. The data from the 7 drop-cast electrodes was then averaged. Uncertainties represent the 95% confidence interval of the mean calculated using the Student's t-distribution.

View Article Online
DOI: 10.1039/D6TA02189A

Associated content

Supporting Information

Additional PDF analysis, Rietveld refinements, SAXS analysis, TEM micrographs, experimental details of the *operando* experiments with data treatment and peak fitting approaches, and electrochemical analysis.

Author information

Corresponding Authors

Kirsten M. Ø. Jensen - Department of Chemistry, University of Copenhagen, Universitetsparken 5, 2100 Copenhagen, Denmark; Orcid https://orcid.org/0000-0003-0291-217X; Email: kirsten@chem.ku.dk

Rebecca K. Pittkowski - Department of Chemistry, University of Copenhagen, Universitetsparken 5, 2100 Copenhagen, Denmark; Orcid https://orcid.org/0000-0002-0351-4993; Email: rebecca.pittkowski@chem.ku.dk

Authors

Laura G. Graversen - Department of Chemistry, University of Copenhagen, Universitetsparken 5, 2100 Copenhagen, Denmark. Orcid https://orcid.org/0000-0002-5964-7744

Freja B. Holde - Department of Chemistry, University of Copenhagen, Universitetsparken 5, 2100 Copenhagen, Denmark.

Nicolas Schlegel - Department of Chemistry, University of Copenhagen, Universitetsparken 5, 2100 Copenhagen, Denmark; Orcid https://orcid.org/0000-0001-7720-3146

Adrian S. Arjona - Department of Chemistry, University of Copenhagen, Universitetsparken 5, 2100 Copenhagen, Denmark; Orcid https://orcid.org/ 0000-0003-3208-5929

Stefanie Punke - Department of Chemistry, University of Copenhagen, Universitetsparken 5, 2100 Copenhagen, Denmark; Orcid https://orcid.org/0000-0001-9896-6265

Tobias M. Nielsen - Department of Chemistry, University of Copenhagen, Universitetsparken 5, 2100 Copenhagen, Denmark; Orcid https://orcid.org/0000-0001-7720-3146

Andy S. Anker - Department of Chemistry, University of Copenhagen, Universitetsparken 5, 2100 Copenhagen, Denmark; Orcid https://orcid.org/ 0000-0002-7403-6642

Jonas Forner - Department of Chemistry, Biochemistry and Pharmaceutical Sciences, University of Bern, Freiestrasse 3, 3012 Bern, Switzerland

Gustav. K. H. Wiberg - Department of Chemistry, Biochemistry and Pharmaceutical Sciences, University of Bern, Freiestrasse 3, 3012 Bern, Switzerland; orcid.org/0000-0003-1884-604X

Matthias Arenz - Department of Chemistry, Biochemistry and Pharmaceutical Sciences, University of Bern, Freiestrasse 3, 3012 Bern, Switzerland; Orcid https://orcid.org/0000-0001-9765-4315; Email: matthias.arenz@unibe.ch

Notes

The authors declare no competing financial interest.

Acknowledgment

We are grateful for support from the Danish National Research Foundation Center for High Entropy Alloy Catalysis (DNRF 149). We are grateful for funding from the Carlsberg Foundation (CF21-0278). We are grateful to the Villum Foundation for financial support (VKR00042079). We thank the Danish Agency for Science, Technology, and Innovation for funding the instrument centre DanScatt. We acknowledge the Diamond Light Source for the provision of synchrotron radiation facilities, and we would like to thank Philip Chater for assistance and support in using beamline I15-1 under proposal CY30653-2. We acknowledge DESY (Hamburg, Germany), a member of the Helmholtz Association HGF, for synchrotron research carried out at beamline P02.1 at Petra III, and we would like to thank Martin Etter for assistance in using the beamline. MAX IV Laboratory for time on the Balder Beamline under Proposal 20220165. Research

View Article Online
DOI: 10.1039/D6TA02189A

conducted at MAX IV, a Swedish national user facility, is supported by the Swedish Research Council under contract 2018-07152, the Swedish Governmental Agency for Innovation Systems under contract 2018-04969, and Formas under contract 2019-02496.

References

1. M. Carmo, D. L. Fritz, J. Mergel and D. Stolten, A comprehensive review on PEM water electrolysis, *Int. J. Hydrogen Energy*, 2013, **38**, 4901-4934.
2. S. Shiva Kumar and V. Himabindu, Hydrogen production by PEM water electrolysis – A review, *Mater. Sci. Energy Technol.*, 2019, **2**, 442-454.
3. J. Rossmeisl, Z. W. Qu, H. Zhu, G. J. Kroes and J. K. Nørskov, Electrolysis of water on oxide surfaces, *J. Electroanal. Chem.*, 2007, **607**, 83-89.
4. M. Povia, D. F. Abbott, J. Herranz, A. Heinritz, D. Lebedev, B.-J. Kim, E. Fabbri, A. Patru, J. Kohlbrecher, R. Schäublin, M. Nachtegaal, C. Copéret and T. J. Schmidt, Operando X-ray characterization of high surface area iridium oxides to decouple their activity losses for the oxygen evolution reaction, *Energy Environ. Sci.*, 2019, **12**, 3038-3052.
5. L. She, G. Zhao, T. Ma, J. Chen, W. Sun and H. Pan, On the Durability of Iridium-Based Electrocatalysts toward the Oxygen Evolution Reaction under Acid Environment, *Adv. Funct. Mater.*, 2022, **32**, 2108465.
6. T. Naito, T. Shinagawa, T. Nishimoto and K. Takanabe, Recent advances in understanding oxygen evolution reaction mechanisms over iridium oxide, *Inorg. Chem. Front.*, 2021, **8**, 2900-2917.
7. H. Dhawan, M. Secanell and N. Semagina, State-of-the-Art Iridium-Based Catalysts for Acidic Water Electrolysis: A Minireview of Wet-Chemistry Synthesis Methods, *Johnson Matthey Technol. Rev.*, 2021, **65**, 247-262.
8. C. Minke, M. Suermann, B. Bensmann and R. Hanke-Rauschenbach, Is iridium demand a potential bottleneck in the realization of large-scale PEM water electrolysis?, *Int. J. Hydrogen Energy*, 2021, **46**, 23581-23590.
9. G. Wu, X. Zheng, P. Cui, H. Jiang, X. Wang, Y. Qu, W. Chen, Y. Lin, H. Li, X. Han, Y. Hu, P. Liu, Q. Zhang, J. Ge, Y. Yao, R. Sun, Y. Wu, L. Gu, X. Hong and Y. Li, A general synthesis approach for amorphous noble metal nanosheets, *Nat Commun*, 2019, **10**, 4855.
10. T. Reier, M. Oezaslan and P. Strasser, Electrocatalytic Oxygen Evolution Reaction (OER) on Ru, Ir, and Pt Catalysts: A Comparative Study of Nanoparticles and Bulk Materials, *ACS Catal.*, 2012, **2**, 1765-1772.
11. H. Jang and J. Lee, Iridium oxide fabrication and application: A review, *J. Energy Chem.*, 2020, **46**, 152-172.
12. A. Marshall, B. Børresen, G. Hagen, M. Tsypkin and R. Tunold, Preparation and characterisation of nanocrystalline $Ir_xSn_{1-x}O_2$ electrocatalytic powders, *Mater. Chem. Phys.*, 2005, **94**, 226-232.
13. Y. Zhao, E. A. Hernandez-Pagan, N. M. Vargas-Barbosa, J. L. Dysart and T. E. Mallouk, A High Yield Synthesis of Ligand-Free Iridium Oxide Nanoparticles with High Electrocatalytic Activity, *J. Phys. Chem. Lett.*, 2011, **2**, 402-406.
14. Y. Lattach, J. F. Rivera, T. Bamine, A. Deronzier and J.-C. Moutet, Iridium Oxide–Polymer Nanocomposite Electrode Materials for Water Oxidation, *ACS Applied Materials & Interfaces*, 2014, **6**, 12852-12859.
15. J. E. Baur and T. W. Spaine, Electrochemical deposition of iridium (IV) oxide from alkaline solutions of iridium(III) oxide, *J. Electroanal. Chem.*, 1998, **443**, 208-216.

View Article Online
DOI: 10.1039/D6TA02189A

16. V. K. Puthiyapura, S. Pasupathi, H. Su, X. Liu, B. Pollet and K. Scott, Investigation of supported IrO2 as electrocatalyst for the oxygen evolution reaction in proton exchange membrane water electrolyser, *Int. J. Hydrogen Energy*, 2014, **39**, 1905-1913.
17. J. Ruiz Esquius, D. J. Morgan, I. Spanos, D. G. Hewes, S. J. Freakley and G. J. Hutchings, Effect of Base on the Facile Hydrothermal Preparation of Highly Active IrO_x Oxygen Evolution Catalysts, *ACS Appl. Energy Mater.*, 2020, **3**, 800-809.
18. N. Bestaoui and E. Prouzet, A Chimie Douce Route to Pure Iridium Oxide, *Chem. Mater.*, 1997, **9**, 1036-1041.
19. G. C. Da Silva, N. Perini and E. A. Ticianelli, Effect of temperature on the activities and stabilities of hydrothermally prepared IrO_x nanocatalyst layers for the oxygen evolution reaction, *Appl. Catal., B*, 2017, **218**, 287-297.
20. J. C. Cruz, V. Baglio, S. Siracusano, R. Ornelas, L. Ortiz-Frade, L. G. Arriaga, V. Antonucci and A. S. Aricò, Nanosized IrO2 electrocatalysts for oxygen evolution reaction in an SPE electrolyzer, *J. Nanopart. Res.*, 2011, **13**, 1639-1646.
21. M. A. Petit and V. Plichon, Anodic electrodeposition of iridium oxide films, *J. Electroanal. Chem.*, 1998, **444**, 247-252.
22. S. Lee, Y.-J. Lee, G. Lee and A. Soon, Activated chemical bonds in nanoporous and amorphous iridium oxides favor low overpotential for oxygen evolution reaction, *Nat. Commun.*, 2022, **13**.
23. M. Elmaalouf, M. Odziomek, S. Duran, M. Gayrard, M. Bahri, C. Tard, A. Zitolo, B. Lassalle-Kaiser, J.-Y. Piquemal, O. Ersen, C. Boissière, C. Sanchez, M. Giraud, M. Faustini and J. Peron, The origin of the high electrochemical activity of pseudo-amorphous iridium oxides, *Nat. Commun.*, 2021, **12**.
24. V. A. Saveleva, L. Wang, D. Teschner, T. Jones, A. S. Gago, K. A. Friedrich, S. Zafeiratos, R. Schlögl and E. R. Savinova, Operando Evidence for a Universal Oxygen Evolution Mechanism on Thermal and Electrochemical Iridium Oxides, *J. Phys. Chem. Lett.*, 2018, **9**, 3154-3160.
25. C. I. Hiley and R. I. Walton, Controlling the crystallisation of oxide materials by solvothermal chemistry: tuning composition, substitution and morphology of functional solids, *CrystEngComm*, 2016, **18**, 7656-7670.
26. K. Sardar, J. Fisher, D. Thompsett, M. R. Lees, G. J. Clarkson, J. Sloan, R. J. Kashtiban and R. I. Walton, Structural variety in iridate oxides and hydroxides from hydrothermal synthesis, *Chem. Sci.*, 2011, **2**, 1573.
27. K. Sardar, S. C. Ball, J. D. B. Sharman, D. Thompsett, J. M. Fisher, R. A. P. Smith, P. K. Biswas, M. R. Lees, R. J. Kashtiban, J. Sloan and R. I. Walton, Bismuth Iridium Oxide Oxygen Evolution Catalyst from Hydrothermal Synthesis, *Chem. Mater.*, 2012, **24**, 4192-4200.
28. A. D. Bertelsen, M. Kløve, N. L. N. Broge, M. Bondesgaard, R. B. Stubkjær, A.-C. Dippel, Q. Li, R. Tilley, M. R. Vogel Jørgensen and B. B. Iversen, Formation Mechanism and Hydrothermal Synthesis of Highly Active $Ir_{1-x}Ru_xO_2$ Nanoparticles for the Oxygen Evolution Reaction, *J. Am. Chem. Soc.*, 2024, **146**, 23729-23740.
29. N. Diklić, A. H. Clark, J. Herranz, D. Aegerter, J. S. Diercks, A. Beard, V. A. Saveleva, P. Chauhan, M. Nachtegaal, T. Huthwelker, D. Lebedev, P. Kayser, J. A. Alonso, C. Copéret and T. J. Schmidt, Surface Ir^{+5} Formation as a Universal Prerequisite for O_2 Evolution on Ir Oxides, *ACS Catal.*, 2023, **13**, 11069-11079.
30. R. A. Flores, C. Paolucci, K. T. Winther, A. Jain, J. A. G. Torres, M. Aykol, J. Montoya, J. K. Nørskov, M. Bajdich and T. Bligaard, Active Learning Accelerated Discovery of Stable Iridium Oxide Polymorphs for the Oxygen Evolution Reaction, *Chem. Mater.*, 2020, **32**, 5854-5863.
31. R. Sharma, M. A. Karlsen, P. Morgen, J. Chamier, D. B. Ravnsbæk and S. M. Andersen, Crystalline Disorder, Surface Chemistry, and Their Effects on the Oxygen Evolution Reaction (OER) Activity of Mass-Produced Nanostructured Iridium Oxides, *ACS Appl. Energy Mater.*, 2021, **4**, 2552-2562.

View Article Online
DOI: 10.1039/D6TA02189A

32. D. González, M. Sodupe, L. Rodríguez-Santiago and X. Solans-Monfort, Metal coordination determines the catalytic activity of IrO_2 nanoparticles for the oxygen evolution reaction, *J. Catal.*, 2022, **412**, 78-86.
33. D. F. Abbott, D. Lebedev, K. Waltar, M. Povia, M. Nachtegaal, E. Fabbri, C. Copéret and T. J. Schmidt, Iridium Oxide for the Oxygen Evolution Reaction: Correlation between Particle Size, Morphology, and the Surface Hydroxo Layer from Operando XAS, *Chem. Mater.*, 2016, **28**, 6591-6604.
34. Y. Lee, J. Suntivich, K. J. May, E. E. Perry and Y. Shao-Horn, Synthesis and Activities of Rutile IrO_2 and RuO_2 Nanoparticles for Oxygen Evolution in Acid and Alkaline Solutions, *J. Phys. Chem. Lett.*, 2012, **3**, 399-404.
35. T. D. Nguyen, G. G. Scherer and Z. J. Xu, A Facile Synthesis of Size-Controllable IrO2 and RuO2 Nanoparticles for the Oxygen Evolution Reaction, *Electrocatalysis*, 2016, **7**, 420-427.
36. S. Billinge and I. Levin, The Problem with Determining Atomic Structure at the Nanoscale, *Science*, 2007, **316**, 561-565.
37. T. L. Christiansen, E. D. Bøjesen, M. Juelsholt, J. Etheridge and K. M. Ø. Jensen, Size Induced Structural Changes in Molybdenum Oxide Nanoparticles, *ACS Nano*, 2019, **13**, 8725-8735.
38. O. Aalling-Frederiksen, M. Juelsholt, A. S. Anker and K. M. Ø. Jensen, Formation and growth mechanism for niobium oxide nanoparticles: atomistic insight from *in situ* X-ray total scattering, *Nanoscale*, 2021, **13**, 8087-8097.
39. M. Juelsholt, A. S. Anker, T. L. Christiansen, M. R. V. Jørgensen, I. Kantor, D. R. Sørensen and K. M. Ø. Jensen, Size-induced amorphous structure in tungsten oxide nanoparticles, *Nanoscale*, 2021, **13**, 20144-20156.
40. T. L. Christiansen, S. R. Cooper and K. M. Ø. Jensen, There's no place like real-space: elucidating size-dependent atomic structure of nanomaterials using pair distribution function analysis, *Nanoscale Adv.*, 2020, **2**, 2234-2254.
41. A. F. Sapnik, C. Sun, J. E. M. Laulainen, D. N. Johnstone, R. Brydson, T. Johnson, P. A. Midgley, T. D. Bennett and S. M. Collins, Mapping nanocrystalline disorder within an amorphous metal–organic framework, *Commun. Chem.*, 2023, **6**.
42. K. M. Ø. Jensen, M. Christensen, P. Juhas, C. Tyrsted, E. D. Bøjesen, N. Lock, S. J. L. Billinge and B. B. Iversen, Revealing the Mechanisms behind SnO_2 Nanoparticle Formation and Growth during Hydrothermal Synthesis: An *In Situ* Total Scattering Study, *J. Am. Chem. Soc.*, 2012, **134**, 6785-6792.
43. X. Yang, A. S. Masadeh, J. R. McBride, E. S. Božin, S. J. Rosenthal and S. J. L. Billinge, Confirmation of disordered structure of ultrasmall CdSe nanoparticles from X-ray atomic pair distribution function analysis, *Phys. Chem. Chem. Phys.*, 2013, **15**, 8480.
44. S. J. L. Billinge and M. G. Kanatzidis, Beyond crystallography: the study of disorder, nanocrystallinity and crystallographically challenged materials with pair distribution functions, *Chem. Commun.*, 2004, 749-760.
45. G. Kwon, S. H. Chang, J. E. Heo, K. J. Lee, J.-K. Kim, B.-G. Cho, T. Y. Koo, B. J. Kim, C. Kim, J. H. Lee, S.-M. Bak, K. A. Beyer, H. Zhong, R. J. Koch, S. Hwang, L. M. Utschig, X. Huang, G. Hu, G. W. Brudvig, D. M. Tiede and J. Kim, Experimental Verification of Ir 5d Orbital States and Atomic Structures in Highly Active Amorphous Iridium Oxide Catalysts, *ACS Catal.*, 2021, **11**, 10084-10094.
46. E. Sadeghi, M. Aaskov Karlsen, V. Karimi, C. Maynau, P. Morgen, R. Sharma, L. Lajaunie and S. M. Andersen, Shaping Low-Iridium $IrRuO_x$ Electrocatalysts with Structural and Electronic Modulation for Proton Exchange Membrane Electrolyzers, *J. Mater. Chem. A*, 2025, **13**, 39841-39858.

View Article Online
DOI: 10.1039/D6TA02189A

47. E. Willinger, C. Massué, R. Schlögl and M. G. Willinger, Identifying Key Structural Features of IrO_x Water Splitting Catalysts, *J. Am. Chem. Soc.*, 2017, **139**, 12093-12101.
48. R. K. Pittkowski, S. Punke, A. S. Anker, A. Bornet, N. P. L. Magnard, N. Schlegel, L. G. Graversen, J. Quinson, A. Dworzak, M. Oezaslan, J. J. K. Kirkensgaard, M. Mirolo, J. Drnec, M. Arenz and K. M. Ø. Jensen, Monitoring the Structural Changes in Iridium Nanoparticles during Oxygen Evolution Electrocatalysis with *Operando* X-ray Total Scattering, *J. Am. Chem. Soc.*, 2024, **146**, 27517-27527.
49. G. K. H. Wiberg, R. K. Pittkowski, S. Punke, O. Aalling-Frederiksen, K. M. Ø. Jensen and M. Arenz, Design and Application of a Gas Diffusion Electrode (GDE) Cell for Operando and *In Situ* Studies, *CHIMIA*, 2024, **78**, 344-348.
50. N. Bestaoui, P. Deniard and R. Brec, Structural Study of a Hollandite-Type KxIrO2, *J. Solid State Chem.*, 1995, **118**, 372-377.
51. O. C. Gagne and F. C. Hawthorne, Bond-length distributions for ions bonded to oxygen: results for the transition metals and quantification of the factors underlying bond-length variation in inorganic solids, *IUCrJ*, 2020, **7**, 581-629.
52. Y. Ping, W. A. Goddard and G. A. Galli, Energetics and Solvation Effects at the Photoanode/Catalyst Interface: Ohmic Contact versus Schottky Barrier, *J. Am. Chem. Soc.*, 2015, **137**, 5264-5267.
53. F. G. Sen, A. Kinaci, B. Narayanan, S. K. Gray, M. J. Davis, S. K. R. S. Sankaranarayanan and M. K. Y. Chan, Towards accurate prediction of catalytic activity in IrO_2 nanoclusters via first principles-based variable charge force field, *J. Mater. Chem. A*, 2015, **3**, 18970-18982.
54. A. A. Bolzan, C. Fong, B. J. Kennedy and C. J. Howard, Structural Studies of Rutile-Type Metal Dioxides, *Acta Crystallogr. Sect. B: Struct. Sci.*, 1997, **53**, 373-380.
55. N. Thakur, Y. Ren, M. Kumar, T. Uchiyama, M. Fujita, I. Arima, M. Ishida, Y. Wu, Y. Tsuji, H. Imai, M. Matsumoto, Y. Zhuang, K. Yamamoto, T. Matsunaga, K. Ohara, M. Matsumoto, Y. Orikasa, Y. Kuroda, S. Mitsushima and Y. Uchimoto, Identifying Active Sites of IrO_x Catalysts for OER: A Combined Operando XAS, SEIRAS, and Theoretical Study, *J. Am. Chem. Soc.*, 2025, **147**, 30613-30625.
56. J.-J. Velasco-Vélez, E. A. Carbonio, C.-H. Chuang, C.-J. Hsu, J.-F. Lee, R. Arrigo, M. Hävecker, R. Wang, M. Plodinec, F. R. Wang, A. Centeno, A. Zurutuza, L. J. Falling, R. V. Mom, S. Hofmann, R. Schlögl, A. Knop-Gericke and T. E. Jones, Surface Electron-Hole Rich Species Active in the Electrocatalytic Water Oxidation, *J. Am. Chem. Soc.*, 2021, **143**, 12524-12534.
57. C. Liang, L. Garcia Verga, B. Moss, S. Kumar, S. B. Scott, M. A. Turner, P. Ferrer, V. Celorrio, D. C. Grinter, Y. Tao, S. Halder, Y. Wang, C. Tseng, G. Yang, G. Held, S. J. Haigh, A. Walsh, I. E. L. Stephens, J. R. Durrant and R. R. Rao, Key role of oxidizing species driving water oxidation revealed by time-resolved optical and X-ray spectroscopies, *Nat. Mater.*, 2026, **25**, 799-807.
58. D. Lebedev, R. Ezhov, J. Heras-Domingo, A. Comas-Vives, N. Kaeffer, M. Willinger, X. Solans-Monfort, X. Huang, Y. Pushkar and C. Copéret, Atomically Dispersed Iridium on Indium Tin Oxide Efficiently Catalyzes Water Oxidation, *ACS Cent. Sci.*, 2020, **6**, 1189-1198.
59. A. Minguzzi, C. Locatelli, O. Lugaresi, E. Achilli, G. Cappelletti, M. Scavini, M. Coduri, P. Masala, B. Sacchi, A. Vertova, P. Ghigna and S. Rondinini, Easy Accommodation of Different Oxidation States in Iridium Oxide Nanoparticles with Different Hydration Degree as Water Oxidation Electrocatalysts, *ACS Catal.*, 2015, **5**, 5104-5115.
60. F. Bizzotto, J. Quinson, A. Zana, J. J. K. Kirkensgaard, A. Dworzak, M. Oezaslan and M. Arenz, Ir nanoparticles with ultrahigh dispersion as oxygen evolution reaction (OER) catalysts: synthesis and activity benchmarking, *Catal. Sci. Technol.*, 2019, **9**, 6345-6356.
61. H. Huang and A. E. Russell, Approaches to achieve surface sensitivity in the *in situ* XAS of electrocatalysts, *Curr. Opin. Electrochem.*, 2021, **27**, 100681.

View Article Online
DOI: 10.1039/D6TA02189A

62. R. K. Pittkowski, Shedding Light on Electrocatalysts: Practical Considerations for *Operando* Studies with High-Energy X-Rays, *ChemElectroChem*, 2024, **11**, e202400171.
63. A. Zagalskaya and V. Alexandrov, Mechanistic Study of IrO_2 Dissolution during the Electrocatalytic Oxygen Evolution Reaction, *J. Phys. Chem. Lett.*, 2020, **11**, 2695-2700.
64. A. Grimaud, A. Demortière, M. Saubanère, W. Dachraoui, M. Duchamp, M.-L. Doublet and J.-M. Tarascon, Activation of surface oxygen sites on an iridium-based model catalyst for the oxygen evolution reaction, *Nat. Energy*, 2016, **2**, 16189.
65. S. Maass, F. Finsterwalder, G. Frank, R. Hartmann and C. Merten, Carbon support oxidation in PEM fuel cell cathodes, *J. Power Sources*, 2008, **176**, 444-451.
66. A.-C. Dippel, H.-P. Liermann, J. T. Delitz, P. Walter, H. Schulte-Schrepping, O. H. Seeck and H. Franz, Beamline P02.1 at PETRA III for high-resolution and high-energy powder diffraction, *J. Synchrotron Radiat.*, 2015, **22**, 675-687.
67. J. Kieffer and D. Karkoulis, PyFAI, a versatile library for azimuthal regrouping, *J. Phys.:Conf. Ser.*, 2013, **425**, 202012.
68. P. Juhás, T. Davis, C. L. Farrow and S. J. L. Billinge, PDFgetX3: a rapid and highly automatable program for processing powder diffraction data into total scattering pair distribution functions, *J. Appl. Crystallogr.*, 2013, **46**, 560-566.
69. P. Juhas, C. L. Farrow, X. Yang, K. R. Knox and S. J. L. Billinge, Complex modeling: a strategy and software program for combining multiple information sources to solve ill posed structure and nanostructure inverse problems, *Acta Crystallogr. Sect. A*, 2015, **71**, 562-568.
70. J. Forner, G. K. H. Wiberg, S. Kausar, A. Maletzko, J. Melke and M. Arenz, Statistical Convergence and Uncertainty in Electrocatalytic Benchmarking of Ir and Ru Oxygen Evolution Catalysts, *ChemRxiv*, 2026, **2026**.

View Article Online
DOI: 10.1039/D6TA02189A

Data availability statement:
Data for this article is available at https://sid.erda.dk/sharelink/e6r8wl0Bm5.